Corrosion Science 54 (2012) 260–269

Contents lists available at SciVerse ScienceDirect

Corrosion Science

journal homepage: www.elsevier.com/locate/corsci

The evolution of crevice corrosion damage on the Ni–Cr–Mo–W alloy-22 determined by confocal laser scanning microscopy

P. Jakupi, J.J. Noël, D.W. Shoesmith *

Department of Chemistry, The University of Western Ontario, London, Ontario, Canada N6A 3K7

ARTICLE INFO

Article history:
Received 2 January 2011
Accepted 20 September 2011
Available online 29 September 2011

Keywords:
A. Nickel
B. Galvanostatic
C. Crevice corrosion
C. Repassivation

ABSTRACT

Crevice corrosion of alloy-22 was studied galvanostatically (10–200 μA) at 120 °C in 5 M NaCl. Corrosion damage was analyzed by confocal laser scanning microscopy to obtain penetration profiles. Three-dimensional images demonstrate that damage morphologies varied with applied current. At low applied currents (⩽70 μA), propagation predominantly leads to penetration into the alloy, whereas at higher applied currents (>70 μA) corrosion damage spreads across the alloy. Limited penetration depths at higher currents are attributed to metal dissolution inhibition by the rapid formation of insoluble molybdates, which force propagation to shift to areas unprotected by molybdate layers.

© 2011 Elsevier Ltd. All rights reserved.

1. Introduction

Ni–Cr–Mo alloys are well known for their exceptional corrosion resistance in a wide range of industrial applications. alloy-22, a commercial Ni–Cr–Mo alloy is especially known for its resistance to localized corrosion processes such as crevice corrosion, pitting corrosion and stress corrosion cracking [1–3]. Since crevice corrosion is one of the most likely localized corrosion modes, this process has been studied in some detail on alloy-22. Such studies include determination of crevice repassivation potentials [4–6], the effects of various inhibitors (i.e., nitrates, sulfates, carbonates, and fluoride) on localized corrosion [4,7–11], and the effects of changes in metallurgical properties arising from various forms of thermal aging [5,9,12–14]. To date, few studies on alloy-22 have focused on the morphology of localized corrosion damage and the depths of corrosion penetration [1], despite their immediate relevance to the assessment of corrosion damage. Two studies have shown that penetration depths increase with applied potential [15] and exposure time [2], but discussion of damage morphology has been limited.

A common form of damage morphology observed in the aggressive environments anticipated within crevices is intergranular corrosion (IGC). For Ni–Cr–Mo alloys, heat-treatment beyond a certain threshold has been shown to lead to the precipitation of secondary phases along grain boundaries [16–19], and these phases have been demonstrated to decrease corrosion resistance [9,19–22].

Mori et al. [22] observed a qualitative relationship between microstructure and corrosion rate for the Ni–Cr–Mo alloys, 22 and 276. It was also suggested that IGC is more likely when relatively higher amounts of secondary phases are present in the bulk matrix of the alloy. In addition, IGC has been observed on crevice corroded alloy-22 specimens where no prior heat-treatment was applied to promote secondary phase formation [1,15,23]. In non-heat treated alloy-22, the preferential localized corrosion observed was attributed to differences in crystallographic orientation of the polycrystal, and no measurable compositional differences were observed between grains and grain boundaries [23].

Previous studies have shown that the extent of crevice corrosion on alloy-22 is limited to negligible damage under natural corrosion conditions [2,24]. The passive potential region on this alloy is ~600 mV in width [25] and the inability to establish active propagation conditions has been attributed to inhibited O_2 reduction kinetics on the passive surface external to the crevice when the corrosion potential is within this range [24]. Because of these slow kinetics, film breakdown sites rapidly repassivate, preventing significant crevice corrosion.

Others have used in situ confocal laser scanning microscopy (CLSM) to examine the morphology of damage accumulation on aluminum AA 2024 T3 alloys [26,27]. In this study, CLSM has been applied to crevice-corroded specimens, initiated and propagated galvanostatically at a number of applied constant currents. CLSM provides a non-contact method to obtain high-resolution (better than 1 μm) three-dimensional images which reveal the surface topography within crevice corroded sites, and permit the determination of corrosion depth profiles without destroying the features

* Corresponding author. Tel.: +1 519 661 2111x86366; fax: +1 519 661 3022.
E-mail address: dwshoesm@uwo.ca (D.W. Shoesmith).

0010-938X/$ - see front matter © 2011 Elsevier Ltd. All rights reserved.
doi:10.1016/j.corsci.2011.09.028

of the corroded region (i.e., corrosion product deposits and etched regions). Our primary objectives are to determine how corrosion damage would accumulate if propagation could be sustained, and to what extent this would be controlled by the chemical conditions established within the crevice, as a consequence of the alloy composition. Since, under galvanostatic conditions, initiation is forced to occur and repassivation is prevented, this approach can be considered very conservative.

2. Experimental

2.1. Electrochemical cell and electrodes

Crevice corrosion experiments were conducted using an electrochemical cell built within a Teflon® (PTFE)-lined Hastelloy pressure vessel [28]. A homemade Ag/AgCl (saturated KCl) reference electrode [29] was used to measure the potential of the working electrode. The working electrode was cut from an alloy-22 plate which was 0.317 cm thick. The alloy composition is given in Table 1. The alloy-22 specimen was machined and bent into a V-shape to ensure that only one crevice was formed in contact with the electrolyte solution, Fig. 1. The crevice assembly was held together with threaded alloy-22 bolts and nuts. The crevice former was a small Teflon wafer sandwiched between the flat metal surface of the working electrode and a Udel® (polysulfone) coupon. This assembly defined a creviced area of ~4 cm^2. The working electrode had a threaded tapped hole in one end to accept a nickel alloy welding rod used to make electrical contact to external circuitry. Udel® bushings were placed between the working electrode and the metal bolts and nuts to insulate the bolts and any additional creviced areas at these locations from the working electrode. The crevice-forming face of the working electrode was ground with a series of wet silicon carbide papers (320, 600, 800, 1000, and 1200 grits). All parts of the crevice assembly were degreased by sonication in methanol and de-ionized water, and then rinsed with de-ionized water, and air dried. Prior to assembly, the V-shaped crevice electrode and Teflon crevice former were submerged in the electrolyte solution to be used, to ensure wetting of the crevice interior. The crevice tightness was adjusted using a Teflon "feeler" strip cut from the same sheet as the Teflon crevice former.

2.2. Experimental procedure

A 5 M NaCl solution, prepared using de-ionized Millipore water (18.2 MΩ cm) and reagent grade sodium chloride (99.0% assay), was used in all experiments. The solution was naturally aerated by agitation in air. To prevent boiling of the electrolyte solution, the electrochemical cell was pressurized with 400 kPa of ultra-high purity argon gas. The temperature was controlled at 120 °C in all experiments. During heat-up, the corrosion potential of the creviced specimen was measured using a Solartron model 1284 potentiostat/galvanostat. All galvanostatic experiments were performed using this same potentiostat/galvanostat. Ten creviced specimens were corroded, each, at a different applied current between 10 and 200 μA, for a time sufficient to accumulate 7 C charge equivalent of corrosion damage.

After each experiment, the creviced specimen was rinsed with de-ionized water and methanol and then dried and stored in a desiccator. The specimens were photographed and examined with an optical microscope (Olympus, IX70). The total crevice corroded area was quantified using image analysis software (Image Pro Plus, version 6.0). CLSM analyses were performed at the University of Virginia, Charlottesville, USA. Analysis was carried out on a Zeiss LSM 510 Microscope. The creviced specimens were fastened to a CLSM stage that allowed for the creviced area to be scanned in three dimensions in order to obtain three dimensional depth profiles. Imaging was performed with an argon laser (488 nm wavelength).

Table 1
Elemental Composition of alloy-22 and alloy-2000 (wt%).

Element	Ni	Cr	Mo	W	Fe	Co	Mn	Si	C	S
Alloy-22	Bal.	22	13	3	3	2.5	0.5	0.08	0.01	0.02

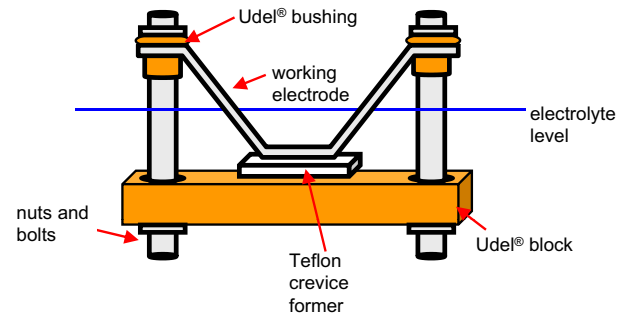

Fig. 1. Schematic of the creviced working electrode (not to scale).

3. Experimental results

3.1. Optical and CLSM images of crevice corroded alloy-22

The electrochemical details of similar experiments have been published elsewhere [24]. On application of a constant current ⩾40 μA, the potential can initially rise to a positive value in excess of 200 $mV_{Ag/AgCl}$ before decreasing, upon the establishment of active crevice corrosion conditions. However, these periods of positive potential are transitory and only minor amounts of transpassive dissolution occur. For lower applied currents the maximum potentials never significantly exceed the upper limit of the passive region prior to the initiation of crevice corrosion. Transpassive corrosion damage on surfaces external to the creviced area was not observed on any specimen.

A region of deepest attack was located optically and chosen as the area for imaging prior to each CLSM scan. Figs. 2–7 show optical micrographs of the crevice corroded region and corresponding 3D CLSM images for six selected specimens representative of the ten crevices corroded at various applied currents. The areas scanned to obtain the CLSM images are outlined with a box on the micrographs. The optical images show that, for all applied currents, crevice initiation and propagation occurred near the crevice edge (mouth).

The CLSM images illustrate the morphology of corrosion damage in more detail. Comparison of the images recorded on the specimens corroded at 10 and 20 μA, Figs.2 and 3b, respectively, shows a distinct variation in damage morphology. The damage on the 10 μA specimen is confined to a small, more deeply penetrated area while damage on the 20 μA specimen is shallower and more widely spread. For specimens corroded at currents in the range 20–70 μA, Figs. 3–5, the distribution of damage varies across the corroded region with a gradation in depth of penetration from locations just inside the crevice mouth to those further into the creviced region. At higher currents (⩾100 μA), Figs. 6 and 7, the depth of penetration close to the crevice mouth is considerably less than that obtained at the lower currents, and corrosion damage is concentrated in a series of pits, commonly coalesced, along the grain boundaries.

The variations in vertical penetration into the specimen with lateral depth into the crevice, and the influence of current upon

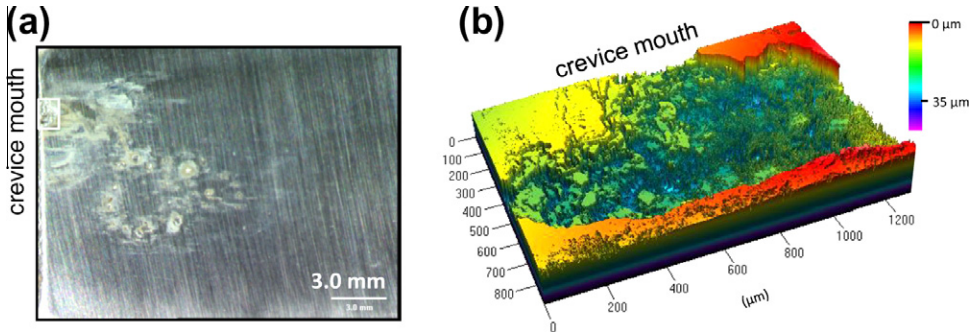

Fig. 2. (a) Optical and (b) corresponding CLSM images (area scanned outlined in white on the optical micrograph) of creviced alloy-22 corroded at a constant current of 10 µA to an accumulated charge of 7 C.

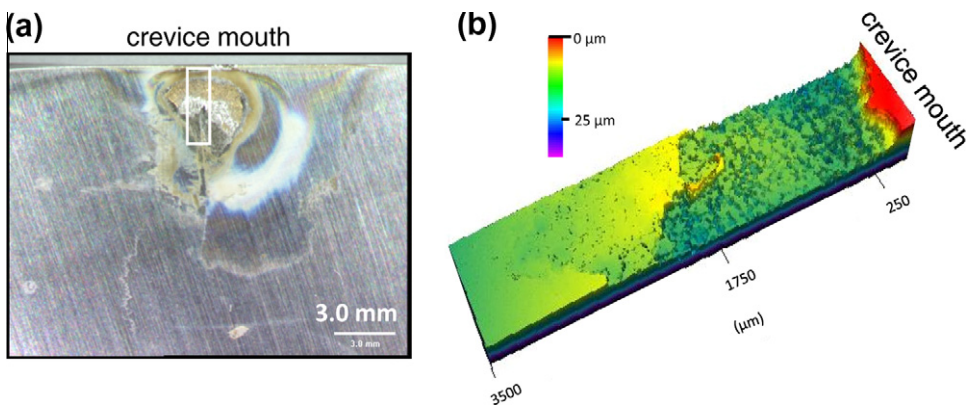

Fig. 3. (a) Optical and (b) corresponding CLSM images (area scanned outlined in white on the optical micrograph) of creviced alloy-22 corroded at a constant current of 20 µA to an accumulated charge of 7 C.

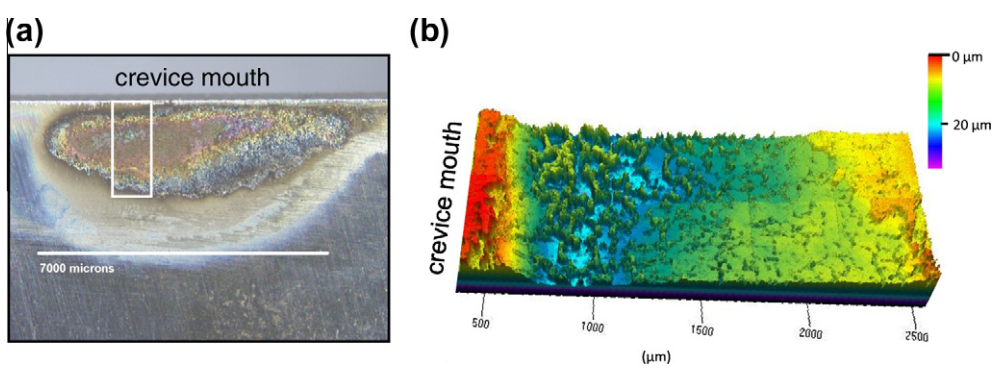

Fig. 4. (a) Optical and (b) corresponding CLSM images (area scanned outlined in white on the optical micrograph) of creviced alloy-22 corroded at a constant current of 40 µA to an accumulated charge of 7 C.

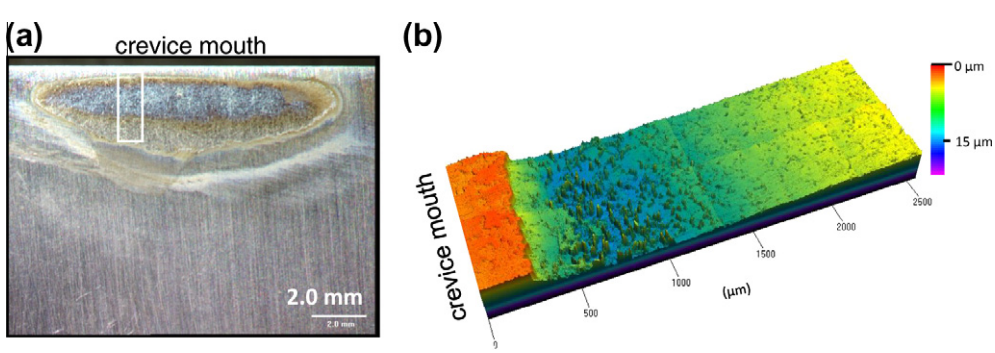

Fig. 5. (a) Optical and (b) corresponding CLSM images (area scanned outlined in white on the optical micrograph) of creviced alloy-22 corroded at a constant current of 70 µA to an accumulated charge of 7 C.

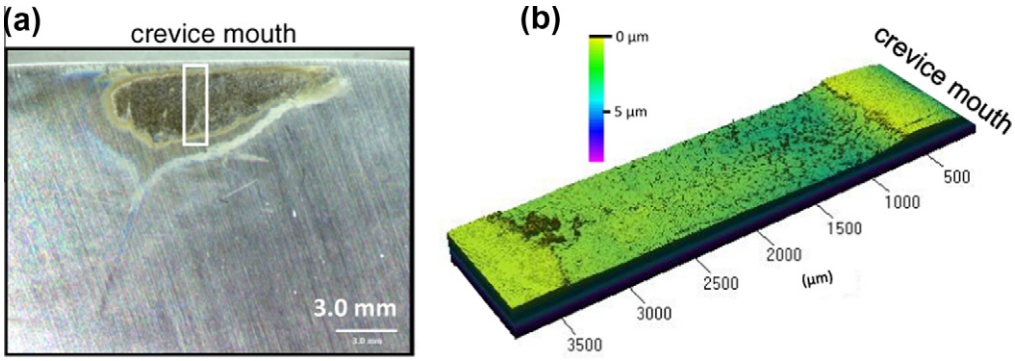

Fig. 6. (a) Optical and (b) corresponding CLSM images (area scanned outlined in white on the optical micrograph) of creviced alloy-22 corroded at a constant current of 100 µA to an accumulated charge of 7 C.

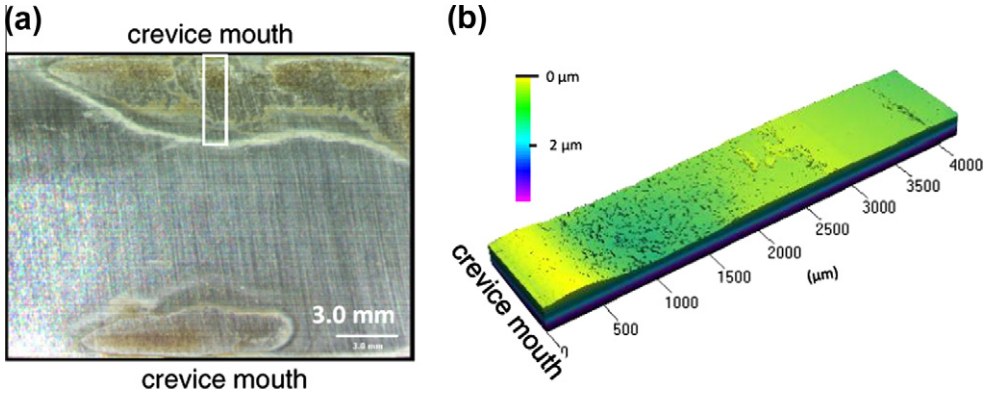

Fig. 7. (a) Optical and (b) corresponding CLSM images (area scanned outlined in white on the optical micrograph) of creviced alloy-22 corroded at a constant current of 200 µA to an accumulated charge of 7 C.

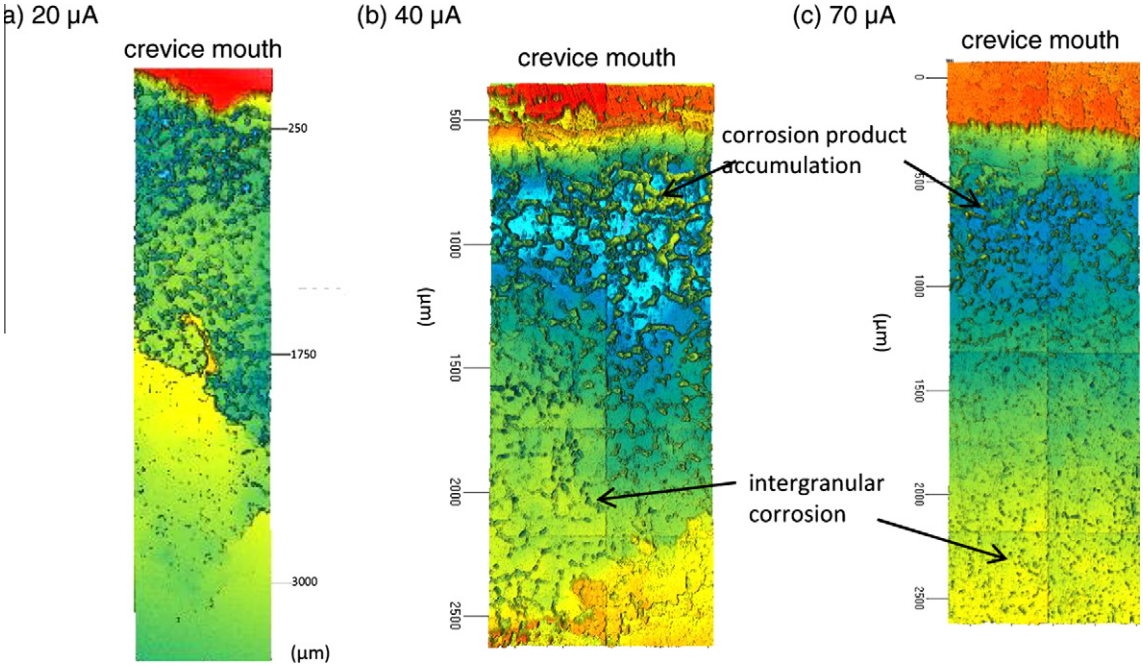

Fig. 8. (a)–(c): Top view CLSM images for coupons corroded at applied currents of (a) 20, (b) 40 and (c) 70 µA.

them, can be more clearly appreciated from the top views of the CLSM images shown in Fig. 8 ((a)–(c)). Penetration depth follows the rainbow color scheme with red being the shallowest and violet the deepest. The region near the crevice mouth accumulates the most concentrated damage, and as the distance from the mouth into the crevice increases, the depth of penetration decreases.

These images show that, at all currents, corrosion in the grain boundaries precedes a more general attack in the deeply penetrated zone close to the crevice mouth and becomes the predominant form of corrosion at locations more remote from the crevice mouth.

Previous studies on the crevice corrosion of alloy-22 have shown different damage morphologies, albeit under different exposure conditions and crevice arrangements, and under potentiostatic rather than galvanostatic polarization. Kehler and Scully [1] and Ilevbare et al. [7] observed small pits that enlarged and coa-

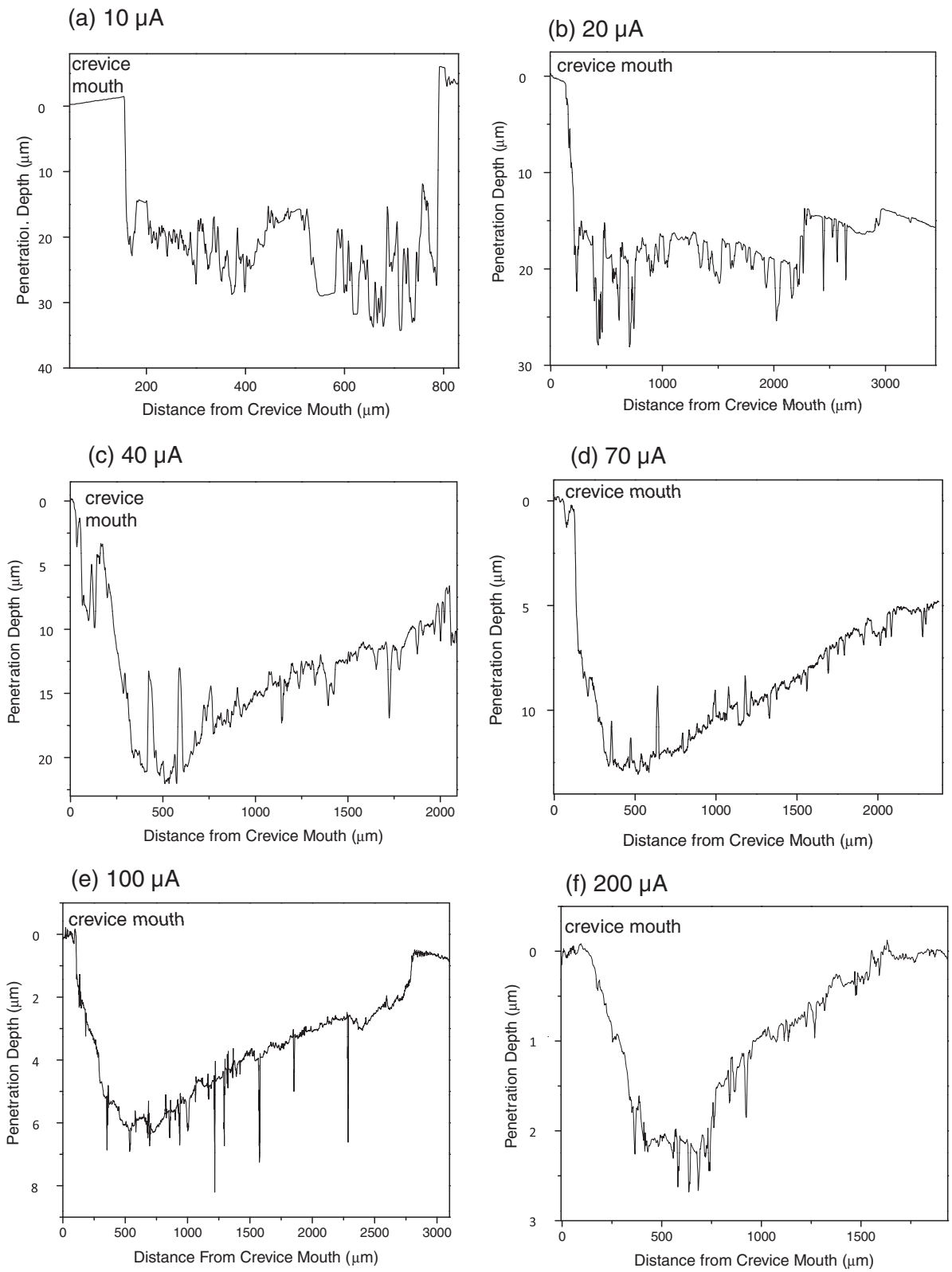

Fig. 9. (a)–(f): Depth profiles corresponding to the CLSM images from Figs. 2–7.

lesced to form trenches, with damage evolving as concentric trenches. As observed in the results presented here, damage was most severe near the crevice mouth and spread towards the center of the crevice. He and Dunn [2] observed that initiation occurred preferentially at the crevice mouth and spread towards the center of the crevice former and to the boldly exposed surface outside the creviced region. The morphology of the damage was not reported, i.e., whether it took the form of pits, trenches, or IGC. In a study to examine the role of metastable pitting [1], creviced specimens of alloy-22 and alloy-625 were polarized to accumulated charges of: 0.005, 0.01, 0.02 and 4 C. At 0.02 C, surface etching and IGC were observed on both alloys near the crevice mouth. When creviced specimens of these two alloys were polarized at 400 $mV_{Ag/AgCl}$ and corroded to an accumulated charge of 4 C, CLSM images revealed deeper corrosion with maximum penetration depths of 120 and 45 μm for alloys 625 and 22, respectively. The damage visible in the CLSM images did not reveal any distinctive morphology and was similar to that observed on the 10 μA creviced specimen, Fig. 2, in this study.

3.2. Depth profiles for crevice corroded specimens at different applied currents

Fig. 9a–f shows depth profiles recorded with a uni-directional CLSM scan across the corroded region, with the location of each scan pre-determined to be near the region of maximum penetration. The depth at the crevice mouth for each depth profile was normalized to 0 μm. The distance (x) from the crevice mouth to the point of maximum penetration was located by examination of the depth profiles and optical micrographs. This parameter is referred to as the critical distance, x_{crit}, and is usually defined in other crevice corrosion studies as the distance from the crevice mouth to the site within the creviced area where the transition from the passive to the active region of the polarization curve is located [30].

In the depth profile of the crevice corroded at 10 μA, Fig. 9a, the slope of the electrode surface just inside the creviced area (0–175 μm) is probably due to either a polishing artefact or to surface etching by the crevice corrosion process. Most of the depth profiles shown in Fig. 9 did not reach the uncorroded area located towards the center of the creviced area. This was due to time constraints imposed when recording the CLSM scans.

Fig. 9a shows large increases in penetration depth for $x > 180$ μm. At deeper locations, penetration is irregular with a maximum penetration depth of ~35 μm. A similar depth profile is observed for the 20 μA specimen (Fig. 9b) although corrosion has spread to considerably deeper locations within the crevice than at the lower current. At these deeper locations the sequence of regular increases and decreases in penetration depth may reflect the IGC attack generally observed.

The depth profiles obtained for specimens corroded at 30–70 μA, are similar (depth profiles are only shown for specimens corroded at 40 and 70 μA, Figs. 9c and d, respectively). Within

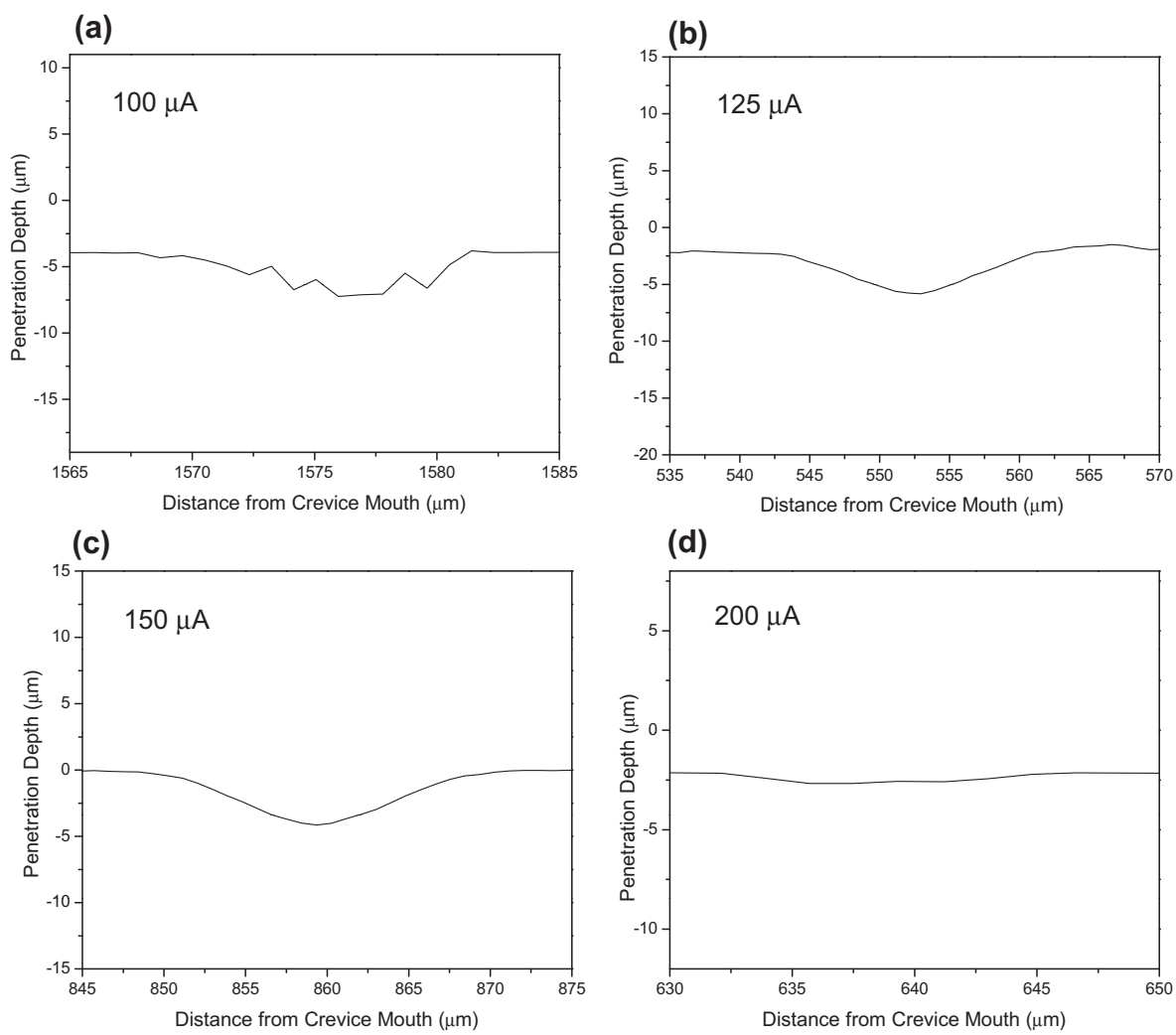

Fig. 10. Normalized depth profile of a corroded grain boundary for creviced specimens subjected to applied currents of (a) 100 μA, (b) 125 μA, (c) and (d) 200 μA.

the area where the maximum penetration depths are located, distinct decreases in depths, appearing as vertical columns, are observed. With increasing distance (x) beyond this location, towards the center of the creviced region, the depth of penetration gradually decreases but is accompanied by sharp localized penetrations. It should be noted that the sharp increases and decreases within the depth profiles, are accentuated by the relative scales used in Fig. 9. The CLSM top view images in Fig. 8 show a decrease in depth (green to yellow shaded areas) within the corroded grain boundaries in the most extensively corroded area (blue shaded area) for specimens corroded at 30, 40, 50, and 70 μA (only shown in Fig. 8b and c for specimens corroded at 40 and 70 μA, respectively). This suggests that the columns observed in the depth profiles are associated with grain boundary locations, indicating a significant degree of grain boundary penetration is disguised beneath corrosion product deposits. Previous Raman analyses [31] have identified these products, formed within grain boundaries in actively propagating crevices, as primarily polymeric molybdates and, to a lesser degree, tungstates. Fig. 8 also verifies that the sharp increase in depths located towards the center of the creviced area are attributed to IGC.

As the applied current is increased, the penetration profiles in the active region within the crevice change markedly; only sharp increases in depth are observed, Figs. 9e and f. This change is clearly visible in the CLSM images (compare specimens corroded at 40 and 70 μA to 100 and 200 μA). This indicates that, along with the decrease in the depth of corrosion, the production of corrosion product deposits decreases within the active location as the current is increased. Once the extent of grain boundary attack is no longer disguised by the corrosion products, it is clear that grain boundary penetration by IGC is significant. However, when the current is increased to 200 μA the depth of IGC, compared to that of general corrosion, is considerably lower. Fig. 10 shows depth profiles for individual pits located on the grain boundaries of specimens subjected to applied currents $\geqslant$100 μA with equally scaled vertical and horizontal axes. It is clear that the morphology of attack is shallow (i.e., the radius of the pit is much greater than the penetration depth) suggesting that although active corrosion takes place at the grain boundaries, it is rapidly inhibited and shifts to other locations within the crevice.

Fig. 11 shows depth profiles for creviced specimens subjected to applied currents of 20–200 μA that have been smoothed by boxcar averaging. These profiles give a clearer view of the magnitude and location of maximum penetration within the corroded region, and show a distinct trend of increasing penetration depth with decreasing applied current. Fig. 12 shows the maximum penetration depths and the total area corroded versus the applied current for creviced specimens polarized to an accumulated charge of 7 C. These plots show that the total area corroded increases linearly, while the maximum penetration depth decreases exponentially, with applied current, indicating that distinct variations in current and potential distribution occur with changes in applied current.

Estimations of x_{crit} measured from optical images and depth profiles for creviced specimens subjected to applied currents in the range 10–200 μA ranged from 500 to 950 μm, but no distinct trend with applied current was observed. This is likely due to variations in the crevice gap caused by surface asperities between the Teflon crevice former and the metal surface. Accurate measurements of x_{crit} have been produced by crevice corrosion studies employing relatively large crevice gaps (100 μm) in a vertical orientation which promotes flushing of the crevice electrolyte [32,33] (i.e., removal of crevice corrosion products), and in studies employing microfabrication techniques to rigorously control crevice gap dimensions [34]. As discussed below, in this study, the true x_{crit} is likely masked by the accumulation of corrosion products during crevice propagation.

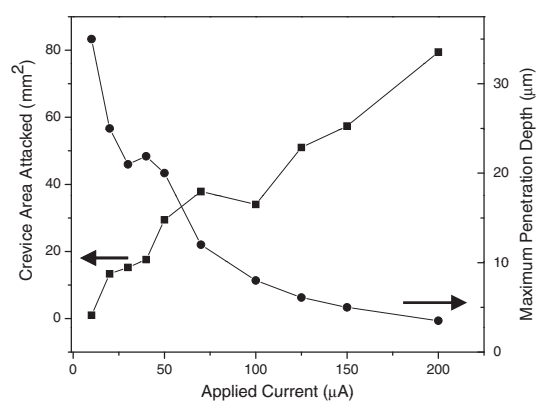

Fig. 12. Total area attacked and maximum penetration depths as a function of applied current for crevice corroded alloy-22 specimens.

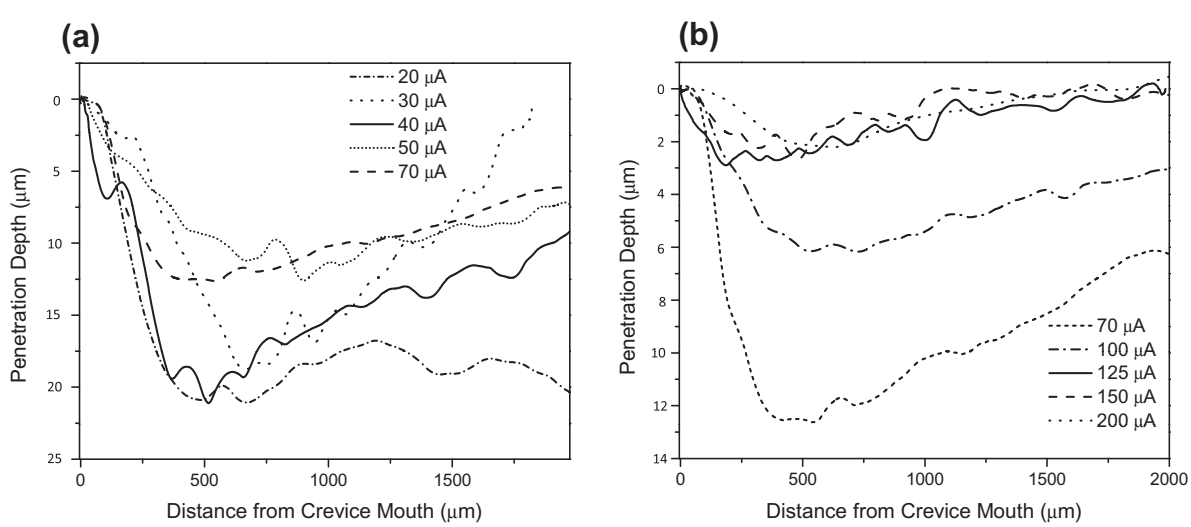

Fig. 11. Boxcar averaged depth profiles corresponding to the CLSM images from Fig. 2 for applied currents of 20–200 μA.

4. Discussion

Crevice damage profiles similar to those presented here have been observed for various other crevice corrosion systems [33–37]. The general depth profile resembles a (reversed) polarization curve for a passive alloy if the distance from the crevice mouth into the crevice is plotted in place of the potential and the penetration depth is plotted in place of the current (e.g., Fig. 1 of Ref. [37]). Three distinct regions may be delineated along the depth profile: the passive region just within the crevice mouth (corresponding to the passive region of the polarization curve), the severely attacked region within which the maximum penetration depth is located (corresponding to the active nose of the polarization curve), and the etched region that is characterized in this study by IGC and accompanied by a decreasing penetration depth at crevice locations towards the middle of the creviced region (corresponding to the transition between the active region and the cathodic region). These regions are related to the potential distribution within the creviced area generated by the IR drop and aggressive chemistry formed.

The IR drop mechanism relates crevice corrosion to the associated IR drop occurring within the creviced area. Provided that this drop is large enough, it can force (lower) the potential within the crevice from values in the passive region into those corresponding to the active region [30]. The IR drop criterion is met when

$$IR > \Delta\Phi^* \quad (1)$$

where I is the ionic current flowing out of the crevice, R is the resistance of the crevice electrolyte, and $\Delta\Phi^*$ is equal to the difference between the potential applied to the creviced electrode, E_{app}, and the potential of the transition between the active and the passive regions, $E_{a/p}$. The active region in passive metal/electrolyte systems is modified by the change in composition of the crevice electrolyte and/or temperature.

x_{crit} may be regarded as the distance from the crevice mouth to the severely attacked area where the location of the active region (i.e., peak current) is expected. Further into the crevice from the mouth, the potential gradient diminishes and approaches a limiting value, Elim, at locations from which no anodic current flows. This defines the inner crevice limit beyond which there is no effect of the applied polarization on the creviced electrode. This distance is referred to as xlim [32]. If xlim is taken to be the point beyond which no damage is observed then it is apparent from the optical images in Figs. 2–7 that crevice attack from the mouth towards the center of the creviced region does not vary much, and is limited with applied current, compared to the lateral spread of attack parallel to the crevice mouth. Thus, as noted in Fig. 12, the evolution of the corroded area is dominated by the lateral spread of damage, a trend that is more pronounced at higher applied currents.

Our previous studies [31], show that insoluble corrosion products, characterized as polymeric molybdates, accumulate within the creviced region. It has been suggested [38] that these species re-enforce passivity by inhibiting the ingress of aggressive species such as Cl^- [39]. Build up of these corrosion products within the crevice may also have a dramatic effect on the crevice IR drop. By constriction of the gap between the crevice former and the alloy surface, they could decrease the effective cross-sectional area of the crevice electrolyte, thus increasing R and, hence, the IR term Equation (1), leading to further stabilization of crevice corrosion [40]. However, the accumulation of corrosion products could also suppress the crevice current [37] by blocking mass transport processes, and eventually destabilize crevice corrosion. This latter effect offers one possible explanation for why crevice corrosion tends to spread laterally parallel to the crevice mouth rather than penetrating more deeply into the crevice.

Fig. 13 shows an optical micrograph of a specimen corroded at an applied current of 70 μA up to an accumulated charge of 3.5 C. Comparison to the micrograph recorded after the accumulation of 7 C at 70 μA, Fig. 5a, demonstrates the tendency of crevice corrosion to propagate laterally parallel to the crevice mouth rather than to locations deeper within the crevice. Fig. 14 compares the penetration depth profiles for the two experiments, and shows that, while damage may spread with time, it also penetrates more deeply. Also, as indicated by the arrow, the location of maximum penetration depth (x_{crit}) moves towards the crevice mouth, a feature that has been attributed to an increase in surface area of the active region due to an increase in current [32]. However, it was later shown for crevices with smaller gap dimensions, that this shift could be primarily attributed to chemical changes within the creviced region [34]. As discussed above, extensive changes in chemical conditions are observed within the crevices in this study.

Fig. 15 shows three penetration depth profiles recorded at an applied current of 200 μA; two for a specimen corroded to an accumulated charge of 7 C and one to 3.5 C. The two profiles for the specimen corroded to a charge of 7 C were recorded on the two damaged areas at the opposite ends of the creviced area shown in Fig. 7a. It is assumed that the crevice in the upper portion of this image initiated much earlier than that in the bottom portion, since

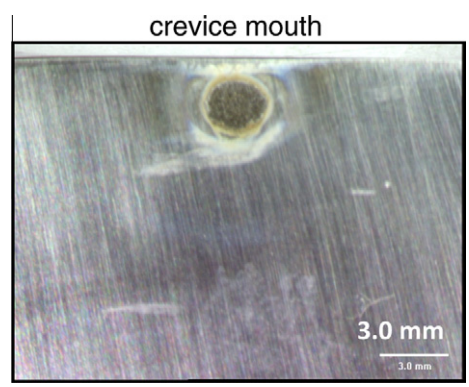

Fig. 13. Optical micrograph of the creviced area for a specimen corroded at an applied current of 70 μA to an accumulated charge of 3.5 C.

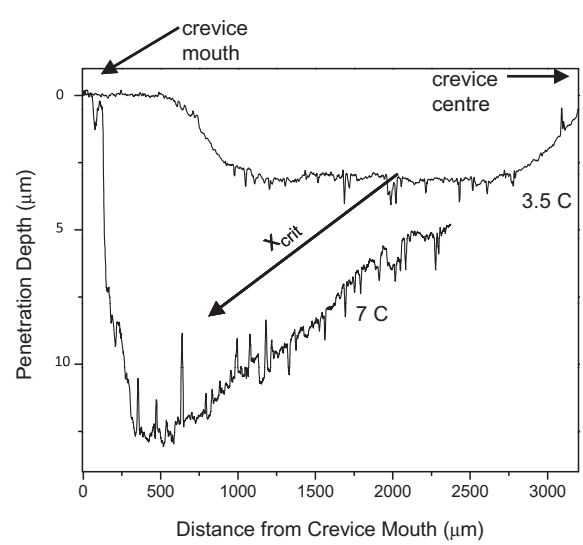

Fig. 14. Depth profiles of creviced specimens corroded at an applied current of 70 μA to accumulated charges of 7 and 3.5 C. Corresponding optical micrographs are shown in Figs. 5 and 13, respectively.

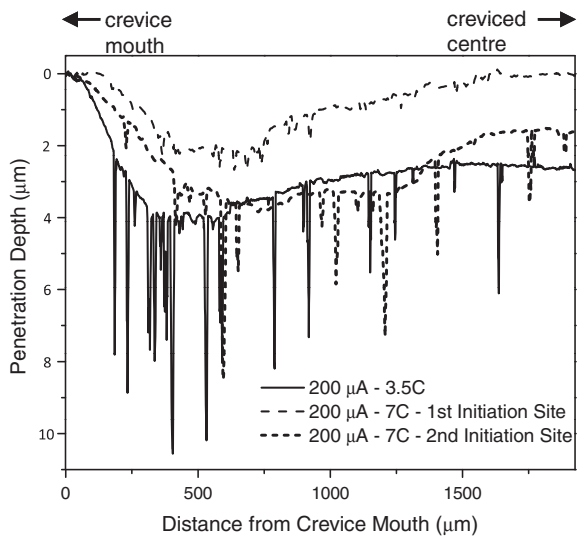

Fig. 15. Depth profiles of creviced specimens corroded at an applied current of 200 μA to accumulated charges of 7 and 3.5 C. The depth profiles for the specimen corroded to 7 C correspond to the top and bottom attacked areas assigned as 1st and 2nd initiation sites, respectively, in Fig. 7.

the accumulated damage is much more extensive and the crevice has spread laterally to a greater degree.

Interestingly, and perhaps counter intuitively, the site assumed to have initiated first shows a smaller penetration depth at locations close to the crevice mouth than that assumed to have initiated second. Since two crevices were propagating simultaneously it is impossible to know what the distribution of current was between them over the duration of the experiment. It is possible that the second initiation site propagated at a much lower current density than the first initiation site. Differences in crevice tightness could also influence the propagation process at the two locations. These differences aside, it is clear that the profiles for the 7 and 3.5 C specimens are not radically different, as they were at the lower current of 70 μA, Fig. 14. As expected, at higher applied currents, IGC sites are obvious and there are no indications of corrosion product deposits, as observed at lower applied currents. Comparison of Figs. 14 and 15 confirms that, with time at the lower applied current, damage tends to accumulate close to the crevice mouth, leading to deep penetration, whereas at higher applied currents corrosion tends to spread with time after causing local, but limited, IGC.

Fig. 16 illustrates schematically how we envisage the distribution of damage to vary with applied current and time. In the early stages of propagation, active corrosion can be locally rapid with the surface unprotected by the presence of molybdates [31], Fig. 16a. At low applied currents, ⩽70 μA, active corrosion can be sustained at these locations, leading to corrosion penetration into the alloy. When the current is increased (⩾100 μA), the current density can only be sustained by spreading, due to the inhibition of metal dissolution by the rapid formation of an insoluble molybdate layer, thus, local penetration does not increase, as illustrated schematically in Fig. 16b. At these applied currents propagation shifts to areas unprotected by a molybdate layer; i.e., at locations peripheral to the active area, and either deeper within the crevice or, as shown in the optical micrographs, along the crevice edge. A similar accumulation of molybdates would inhibit propagation within grain boundaries, leading to only shallow pit formation, as demonstrated in Fig. 10.

Various other morphologies for damage accumulation within active crevices have been observed or proposed, but these generally have been created under potentiostatic conditions when the available current for propagation is effectively unlimited [11,41]. These studies also showed that the penetration depth varied with position within the crevice, indicating a non-uniform distribution of current density. It was also shown in galvanically–coupled experiments stimulated by the addition of $CuCl_2$ [2] that penetration rates decreased with time, eventually leading to stifling or repassivation. The mechanism for repassivation was not discussed, although it was suggested that the formation of salt films inhibited corrosion.

In this study, the constant current approach was chosen in an attempt to control the available current for metal dissolution, since we have previously shown that one key limiting factor in the crevice corrosion of alloy 22 is the slow kinetics of O_2 reduction on passive surfaces outside the crevice [24]. Despite the obvious

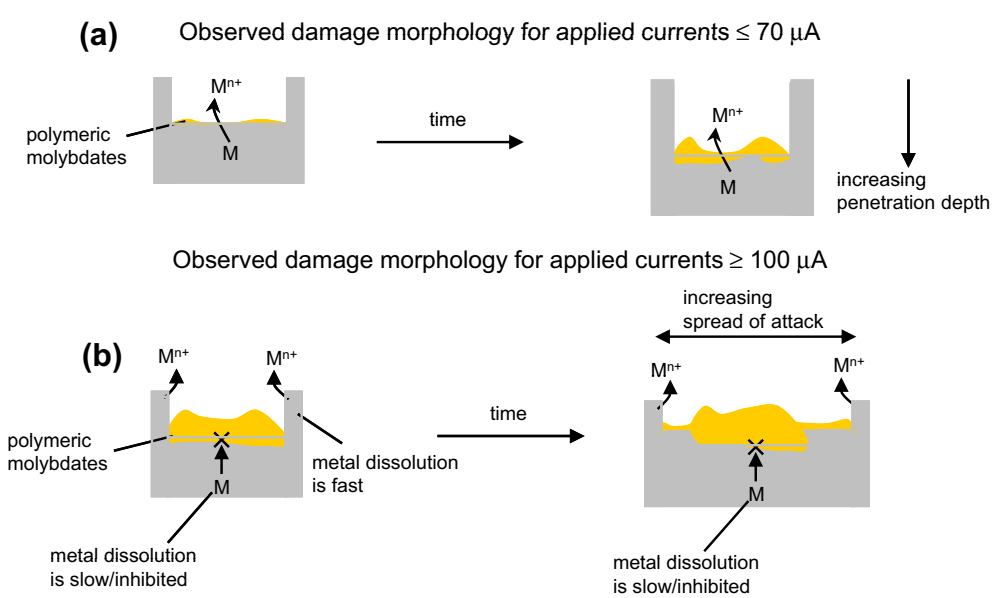

Fig. 16. Schematics demonstrating varying damage morphologies for low (a) and higher (b) applied currents as a consequence of polymeric molybdate formation within the active region.

limitation of this approach, the prevention of repassivation, we believe our results represent the damage distribution features that would be observed if oxidant reduction could be sustained and passivation avoided. Other crevice corrosion studies have demonstrated, via ex situ analyses, that the alloying elements, Mo and W, are enriched in crevice-damaged regions [15,42], and these and our previous study [31] have shown that the presence of molybdates impedes crevice propagation at higher rates, leading to a redistribution of current density within the crevice-corroding region. This effect could explain the observations of Kehler and Scully [1] who showed that, in comparison to alloy-22, alloy-625 (containing only 8.88 wt% Mo compared to 13.05 wt% for alloy-22 (Table 1)) experienced considerably greater crevice penetration depths.

The alternative explanation for the influence of Mo on localized corrosion [41,43,44], that Mo suppresses active metal dissolution on the alloy surface, is not supported, but unfortunately not ruled out, by our observations. While congruent dissolution of alloying elements is generally observed [45,46] Mo and W are primarily retained at the corroding location, while Ni and Cr are predominantly transported away from the active region. Our evidence presented here favors the argument that damage distribution is controlled by local anodic current density, which is regulated by the accumulation of molybdate films at active locations. Our electrochemical studies [24] indicate that there is a threshold current density below which propagation cannot be maintained. These combined studies suggest that, while the molybdate film may strongly influence the distribution of crevice corrosion damage, it is the slow kinetics of O_2 reduction which leads to inevitable repassivation of alloy 22.

5. Conclusions

The crevice corrosion of alloy-22 in 5 M NaCl has been studied under galvanostatic conditions at various applied currents and the distribution and penetration depth of corrosion damage determined by CSLM. At high applied currents (appreciable propagation rates), the accumulation of insoluble corrosion products inhibits penetration leading to the spread of damage across the creviced surface. At low applied currents (low propagation rates) the propagation rate can be sustained locally, leading to deeper crevice penetration. The maximum penetration depth was shown to be inversely proportional to both the damaged area and the applied current.

Acknowledgments

The authors thank the Science and Technology Program of the Office of the Chief Scientist (OCS), Office of Civilian Radioactive Waste Management (OCRWM), and the United States Department of Energy (DOE) for support. The work was performed under the Corrosion and Materials Performance Cooperative, DOE Cooperative Agreement No. DE-FC28-04RW12252. The views and opinions of the authors expressed herein do not necessarily state or reflect those of the United States Department of Energy.

The authors would also like to thank Andrew Hodges and Rob Kelly for use of the CLSM instrument and facilities at the Centre of Electrochemical Science and Engineering, Charlottesville, Virginia, USA.

References

[1] B.A. Kehler, J.R. Scully, Corrosion 61 (2005) 665–684.
[2] X. He, D.S. Dunn, Corrosion 63 (2007) 145–158.
[3] K.T. Chiang, D.S. Dunn, G.A. Cragnolino, Corrosion 63 (2007) 940–950.
[4] B.A. Kehler, G.O. Ilevbare, J.R. Scully, Corrosion 57 (2001) 1042–1065.
[5] K.J. Evans, A. Yilmaz, S.D. Day, L.L. Wong, J.C. Estill, R.B. Rebak, JOM 57 (2005) 56–61.
[6] A.K. Mishra, G.S. Frankel, Corrosion 64 (2008) 836–844.
[7] G.O. Ilevbare, K.J. King, S.R. Gordon, H.A. Elayat, G.E. Gdowski, T.S.E. Summers, J. Electrochem. Soc. 152 (2005) B547–B554.
[8] R.B. Rebak, Mater. Res. Soc. Symp. Proc., Boston, MA, November/December 27-1, 985, (2007) 261–268.
[9] D.S. Dunn, Y.M. Pan, K.T. Chiang, L. Yang, G.A. Cragnolino, X. He, JOM 57 (2005) 49–55.
[10] G.O. Ilevbare, Corrosion 62 (2006) 340–356.
[11] R.M. Carranza, M.A. Rodriguez, R.B. Rebak, Corrosion 63 (2007) 480–490.
[12] R.B. Rebak, Metallurgical effects on the corrosion behaviour of nickel alloys, in: S.D. Cramer, B.S. Covino Jr., (Eds.), ASM Metals Handbook, 13A, Corrosion: Fundamental, Testing, and Protection, Materials Park, OH, (2003) 279–286.
[13] D.S. Dunn, Y.M. Pan, L. Yang, G.A. Cragnolino, Corrosion 62 (2006) 3–12.
[14] R.B. Rebak, R.A. Etien, S.R. Gordon, G.O. Ilevbare, Corrosion 62 (2006) 967–980.
[15] M.A. Rodriguez, R.M. Carranza, R.B. Rebak, Corrosion 66 (2010) 1–14.
[16] M. Raghavan, B.J. Berkowitz, J.C. Scanlon, Metall. Trans. A 13 (1982) 979–984.
[17] H.M. Tawancy, J. Mater. Sci. 31 (1996) 3929–3936.
[18] T.S.E. Summers, M.A. Wall, M. Kumar, S.J. Mathews, R.B. Rebak, Mater. Res. Soc. Symp. Proc., Boston, MA, 29-2 556 (2000) 919–926. Nov./Dec.
[19] U.L. Heubner, E. Altpeter, M.B. Rockel, E. Wallis, Corrosion 45 (1989) 249–259.
[20] R.B. Rebak, T.S.E. Summers, R.M. Carranza, Mater. Res. Soc. Symp. Proc., Boston, MA, November/December, 29-2, 608, 2000, 109–114.
[21] T.S.E. Summers, R.B. Rebak, T.A. Palmer, P. Crook, Mater. Res. Soc. Symp. Proc., Boston, MA, 26-29, November, 713, 2002, 45–52.
[22] G. Mori, S. Sutthiruangwong, M. Czerny, T. Partlic, Corrosion 60 (2004) 1082–1091.
[23] P. Jakupi, J.J. Noël, D.W. Shoesmith, Electrochem. Solid-State Lett. (13) (2010) C1–C3.
[24] P. Jakupi, J.J. Noël, D.W. Shoesmith, Corros. Sci. 53 (2011) 3122–3130.
[25] P. Jakupi, D. Zagidulin, J.J. Noël, D.W. Shoesmith, Electrochim. Acta. 56 (2011) 6251–6259.
[26] G.O. Ilevbare, O. Schneider, R.G. Kelly, J.R. Scully, J. Electrochem. Soc. 151 (2004) B453–B464.
[27] O. Scheider, G.O. Ilevbare, J.R. Scully, R.G. Kelly, J. Electrochem Soc. 151 (2004) B465–B472.
[28] X. He, J.J. Noël, D.W. Shoesmith, Corros. Sci. 47 (2005) 1177–1195.
[29] J.J. Noël, Ph.D Thesis, Dept. of Chem., University of Manitoba, Winnipeg Manitoba (1999).
[30] H.W. Pickering, J. Electrochem Soc. 150 (2003) K1–K13.
[31] P. Jakupi, F. Wang, J.J. Noël, D.W. Shoesmith, Corros. Sci. 53 (2011) 1670–1679.
[32] M.I. Abdulsalam, H.W. Pickering, J. Electrochem. Soc. 145 (1998) 2276–2284.
[33] M.I. Abdulsalam, H.W. Pickering, Corros. Sci. 41 (1999) 351–372.
[34] J.S. Lee, M.L. Reed, R.G. Kelly, J. Electrochem. Soc. 151 (2004) B423–B433.
[35] K. Cho, H.W. Pickering, J. Electrochem. Soc. 138 (1991) L56–L58.
[36] E.A. Nystrom, J.B. Lee, A.A. Sagüés, H.W. Pickering, J. Electrochem. Soc. 141 (1994) 358–361.
[37] J.N. Al-Khamis, H.W. Pickering, J. Electrochem. Soc. 148 (2001) B314–B321.
[38] R.S. Lillard, M.P. Jurinski, J.R. Scully, Corrosion 50 (1994) 251–265.
[39] Y.C. Lu, C.R. Clayton, A.R. Brooks, Corros. Sci. 29 (1989) 863–880.
[40] A.M. Al-Zahrani, H.W. Pickering, Electrochim. Acta 50 (2005) 3420–3435.
[41] F. Bocher, F. Presuel-Moreno, J.R. Scully, J. Electrochem. Soc. 155 (2008) C256–C268.
[42] X. Shan, J.H. Payer, J. Electrochem. Soc. 156 (2009) C13–C321.
[43] R.C. Newman, Corros. Sci. 25 (1985) 331–339.
[44] R.C. Newman, Corros. Sci. 25 (1985) 341–350.
[45] A.C. Lloyd, J.J. Noël, S. McIntyre, D.W. Shoesmith, Electrochim. Acta 49 (2004) 3015–3027.
[46] A.C. Lloyd, J.J. Noël, S. McIntyre, D.W. Shoesmith, J. Electrochem. Soc. 150 (2003) B120–B130.